RSC Advances

PAPER

View Article Online
View Journal | View Issue

Cite this: *RSC Adv.*, 2026, **16**, 15979

Upcycling sawdust into sustainable binder-free nitrogen-doped carbon nanofiber electrodes for high energy density supercapacitors

Dalia M. El-Gendy,[ac] Hebat-Allah S. Tohamy [b] and Ehab N. El Sawy *[c]

Received 19th January 2026
Accepted 17th March 2026

DOI: 10.1039/d6ra00480f

rsc.li/rsc-advances

Electrochemical supercapacitors (ESCs) are emerging as key energy storage systems, enabling the integration of renewable energy and powering the next generation of electric vehicles. In this study, we present a sustainable and innovative approach to high-performance electrode materials by transforming pinewood sawdust (PWSD), an abundant agricultural waste, into carbon nanotubes/nanofibers (CNTs/CNFs) and then into nitrogen-doped carbon nanofibers (N-CNFs). The CNTs/CNFs and N-CNFs were rigorously characterized using XRD, FT-IR, TGA, EDS, XPS, SEM, and TEM, confirming their successful synthesis and robust structural integrity. Electrochemical evaluation through cyclic voltammetry (CV), galvanostatic charge/discharge (GCD), and electrochemical impedance spectroscopy (EIS) revealed exceptional performance of the N-CNFs. The N-CNF electrode achieved a remarkable specific capacitance of ≈1280 F g^{-1} at 1 A g^{-1}. Furthermore, an assembled symmetric supercapacitor device delivered an outstanding energy density of 78.3 Wh kg^{-1} and a power density of 750 W kg^{-1}, along with exceptional cycling stability, with 100% capacitance retention after 4000 cycles. This superior performance is attributed to the synergistic combination of high electrical conductivity, nanofiber architecture, and enhanced surface wettability. Our findings underscore the significant potential of this waste-derived composite as a premier electrode material for building high-capacity, sustainable electrochemical supercapacitors.

1. Introduction

Energy is a fundamental driver of human development and economic growth. Yet, the ever-increasing global demand for energy raises pressing concerns about resource scarcity and sustainability. Reliance on conventional fossil fuels is no longer viable, as these finite resources are the primary contributors to greenhouse gas emissions.[1] Renewable alternatives such as solar, wind, and hydropower offer a cleaner and more sustainable path forward. However, their inherent intermittency underscores the urgent need for efficient storage technologies that can reliably harness and stabilize these resources to meet future energy demands.[2]

To address this challenge, a broad range of energy storage technologies, including batteries, fuel cells, capacitors, and supercapacitors, is being extensively explored. Among them, supercapacitors have attracted considerable attention due to their unique combination of high-power density, rapid charge/discharge rates, excellent reversibility, and outstanding long-term cycling stability. Depending on their charge storage mechanism, supercapacitors are generally classified as electrical double-layer capacitors (EDLCs), pseudocapacitors, or hybrid supercapacitors.[3] EDLC-based materials offer high power density and extended cycle life. In contrast, pseudocapacitive materials, although capable of achieving higher specific capacitance, often suffer from structural degradation caused by repeated redox reactions, which limits their long-term durability.[4,5] Hybrid supercapacitors, by integrating both mechanisms, aim to balance high energy density with reliable cycling performance.

In this context, carbon-based materials, including activated carbon (AC), graphite, graphene oxide (GO), graphene oxide nanoribbons (GONRs), carbon nanotubes (CNTs), and carbon nanofibers (CNFs), have emerged as leading candidates.[6–11] Their versatility, tunable properties, and compatibility with diverse operating conditions make them especially attractive. Recent efforts have focused on engineering these materials to enhance their electrochemical behavior, particularly by exploiting hybrid supercapacitance mechanisms, thereby enabling the development of cost-effective, high-performance, and sustainable energy storage devices.

Carbon nanotubes (CNTs) and carbon nanofibers (CNFs) are widely regarded as premier candidates for high-performance supercapacitors, owing to their excellent electrical conductivity, well-defined porosity, and mechanical robustness,

[a]*Physical Chemistry Department, National Research Centre, Dokki, Giza, 1262, Egypt*
[b]*Cellulose and Paper Department, National Research Centre, Dokki, Giza, 12622, Egypt*
[c]*Department of Chemistry, School of Science and Engineering, The American University in Cairo, New Cairo, Cairo, 11835, Egypt. E-mail: ehab.elsawy@aucegypt.edu*

features that make them ideal for ultra-high power and flexible energy storage devices.[12,13] Nevertheless, their large-scale adoption is constrained by challenges in cost-effective, scalable production. In this context, upcycling waste biomass into carbon-based materials offers a sustainable and economical alternative for fabricating supercapacitor electrodes.

Beyond structural optimization, heteroatom doping has emerged as a powerful strategy to further enhance the electrochemical performance of carbon-based electrodes. Nitrogen doping has been shown to significantly enhance capacitance. For example, optimizing nitrogen content can increase the specific capacitance by more than threefold compared to undoped samples.[14] Zhao *et al.* demonstrated that nitrogen-doped CNFs derived from biomass exhibited electrochemical performance approximately 2.7 times higher than that of commercial CNTs,[15] primarily due to the incorporation of pyridinic and graphitic nitrogen, which introduced abundant active sites.[15] This enhancement is attributed to the synergistic effect of increased pseudocapacitance and improved electrical conductivity, as well as the improved wettability imparted by nitrogen functionalities, which facilitate faster ion transport through micropores.[14] Furthermore, nitrogen atoms can donate their lone electron pair to the delocalized π-system, generating additional negative charges that strengthen interactions between carbon structures and electrolyte ions, thereby improving overall electrode performance.[16]

Pinewood sawdust, a byproduct of the wood industry, represents an abundant and low-cost biomass precursor with significant potential for valorization into advanced carbon materials.[17] Previous studies have demonstrated its applicability; for instance, Lei *et al.* successfully synthesized CNTs from pine sawdust using a CVD method,[18] while other reports utilized pine sawdust-derived activated carbon for supercapacitors, achieving a capacitance of 176 F g^{-1} and an energy density of 24.4 Wh kg^{-1} at 0.5 A g^{-1}.[19]

Building on these foundations, the present study introduces an effective, *in situ* strategy for converting pinewood sawdust into nitrogen-doped carbon nanofibers. This sustainable approach not only transforms a widely available waste material into a valuable electrode resource but also advances green pathways in energy storage technologies. Emphasis is placed on elucidating the role of nitrogen species derived from urea in modulating electrochemical performance, including specific capacitance, energy density, and power density. The incorporation of nitrogen provides additional pseudocapacitance, enhancing charge storage behavior and resulting in significantly improved energy storage capabilities and elevated capacitance values.

2. Experimental

2.1. Materials and chemicals

Iron(III) nitrate hydrate $Fe(NO_3)_3 \cdot 9H_2O$, nickel(II) nitrate hydrate $Ni(NO_3)_3 \cdot 6H_3O$, cobalt(II) nitrate hydrate $Co(NO_3)_2 \cdot 6H_2O$, urea, aluminum hydroxide $Al(OH)_3$, nitric acid HNO_3, and sulfuric acid H_2SO_4. 99% were all purchased from Sigma-Aldrich. Pinewood sawdust (PWSD), used as the carbon precursor, was collected from local carpentry shops in Egypt.

2.2. Conversion of pinewood sawdust (PWSD) to CNTs/CNFs and N-CNFs

Carbon nanotubes/nanofibers CNTs/CNFs were prepared using pinewood sawdust (PWSD) as a carbon precursor. A total of 5 g of (PWSD) was mixed with an aqueous solution containing 10 wt% $Fe(NO_3)_3 \cdot 9H_2O$, 10 wt% $Ni(NO_3)_3 \cdot 6H_3O$, and 5 wt% $Co(NO_3)_2 \cdot 6H_2O$, along with 10 wt% urea. The mixture was subjected to hydrothermal treatment at 180 °C for 3 h, and the resulting hydrochar was filtered, washed with distilled water, and dried. A catalyst of $Al_2O_3/FeNiO_x$ was prepared, to further induce the formation of fiber-like structure, by impregnating aluminum hydroxide ($Al(OH)_3$) with 5 wt% $Fe(NO_3)_3 \cdot 9H_2O$ and $Ni(NO_3)_3 \cdot 6H_3O$, followed by calcination at 750 °C for 2 h. The dried hydrochar was physically mixed with the catalyst at a 10 : 1 mass ratio by grinding and thermally treated at 800 °C for 1 h in a closed stainless-steel reactor. This two-step protocol of hydrothermal impregnation of Fe, Ni, and Co, followed by catalytic pyrolysis to synthesize carbon nanofibers from biomass, is an established valorization strategy.[20,21] Initially, PWSD impregnation with the transition metal salts and urea under hydrothermal conditions promotes porosity and uniform metal dispersion within the hydrochar precursor, facilitating subsequent nanofiber nucleation. The complementary $Al_2O_3/FeNiO_x$ catalyst provides stable bimetallic nanoparticles that synergistically guide graphitic fiber growth during pyrolysis at 800 °C, consistent with transition-metal-catalyzed mechanisms in which particle size dictates diameter *via* tip- and base-growth.[22] The final product was purified by removing the catalyst and any remaining metal oxides using sequential washing with 5 M HNO_3 and H_2SO_4, followed by rinsing with hot distilled water and drying.[23]

For the preparation of nitrogen-doped carbon nanofibers (N-CNFs), 0.5 g of the prepared CNTs/CNFs was mixed with 0.60 g of urea in 30 mL of ethanol and sonicated for 30 minutes. Subsequently, the mixture was heated at 350 °C for 5 hours in a muffle furnace. The resulting black powder was washed with ethanol and deionized water multiple times, then dried in an oven at 60 °C overnight for further use.[24]

2.3. Characterization

FTIR analysis was conducted using a Mattson 5000 spectrometer (Unicam, United Kingdom) with the KBr disk method. The crystal structure of the synthesized materials was investigated using X-ray diffraction (XRD) (XPERT-PRO-Analytical), with Cu Kα radiation source ($\lambda = 1.54$ Å). Parameters such as the crystalline index (Cr. I; eqn (1)), *d*-spacing (eqn (2)), crystallite size, dislocation density, and macrostrain were addressed.

$$\text{Cr. I}(\%) = \frac{S_c}{S_t} \times 100 \quad (1)$$

$$d(\text{nm}) = \frac{\lambda}{2 \sin \theta} \quad (2)$$

where S_c = area of the crystalline domain, S_t = area of the total domain, θ = Bragg's angle in radians, and λ = X-ray wavelength (0.1542 nm).[25–27] A TGA examination was performed using a Q50 thermogravimetric analyzer at a heating rate of 10 °C min^{-1}

under a N_2 atmosphere to 800 °C. Sample morphology was examined using scanning electron microscopy (SEM, Quanta-250) and a high-resolution transmission electron microscope (HRTEM, JEOL JEM-2100) operating at 120 kV. Energy-dispersive X-ray spectroscopy (EDS) and EDS mapping were performed to determine the composition of the synthesized material and its composite, using a bench-top Neoscope JCM-6000 Plus from JEOL. For EDS measurements, the samples were placed on a Cu plate and not mounted with carbon tape to avoid substrate effects. X-ray photoelectron spectroscopy (XPS) was used to further confirm the composition, using SPECS Surface Nano Analysis GmbH (Germany), Version 4.89.2-r104748, with Al-Kα radiation and a 500 μm beam size. The Raman spectra were obtained from single-point measurements using a confocal Raman microscope (WITec Alpha 300RA, made in Germany) with a 532 nm excitation laser at 5 mW. The laser spot size was ~1 μm, and each measurement was collected with a 30 s integration time and 10 accumulations at the same point. The measurements were repeated multiple times, and the reported spectrum represents the average, yielding a reliable and representative Raman spectrum.

2.4. Electrode fabrication and electrochemical measurements

All electrochemical tests were performed using a three-electrode setup, in which the working electrode was prepared by coating a graphite sheet with an ink of CNTs/CNFs or N-CNFs in deionized water, serving as a binder-free electrode. A saturated calomel electrode (SCE) served as the reference electrode, and a platinum wire as the counter electrode. The electrochemical experiments were conducted in 0.5 M H_2SO_4 using a Biologic SP-300 Potentiostat. Cyclic voltammetry (CV) experiments were conducted over a potential range of 0.0–1.2 V *vs.* SCE at scan rates of 5 to 100 mV s^{-1}. Galvanostatic charge/discharge (GCD) experiments were performed at current densities of 1–10 A g^{-1}, using potential limits of 0 and 1.2 V *vs.* SCE. Electrochemical impedance spectroscopy (EIS) was measured at the open-circuit potential (OCP) over the frequency range of 0.01 Hz to 100 kHz with an amplitude of 5 mV.

A symmetrical supercapacitor device was assembled using 0.5 M H_2SO_4 as the electrolyte and filter paper as the separator, with N-CNFs as both the negative and positive electrodes. The device supercapacitance performance was evaluated using CV (different scan rates) and GCD (different current densities) using a potential window of 1.5 V, with the EIS being measured at OCP in the frequency range of 0.01 Hz to 100 kHz.

3. Results and discussion

3.1. Physical and chemical characterizations

The morphology and elemental composition of the carbon nanotubes/nanofibers (CNTs/CNFs) and nitrogen-doped nanofibers (N-CNFs) were examined using FE-SEM, EDS (spot and mapping analysis), and the results are displayed in Fig. 1. Fig. 1a depicts a randomly oriented structure with uniform tube diameters of CNTs/CNFs in the range of 26 nm to 33 nm. While

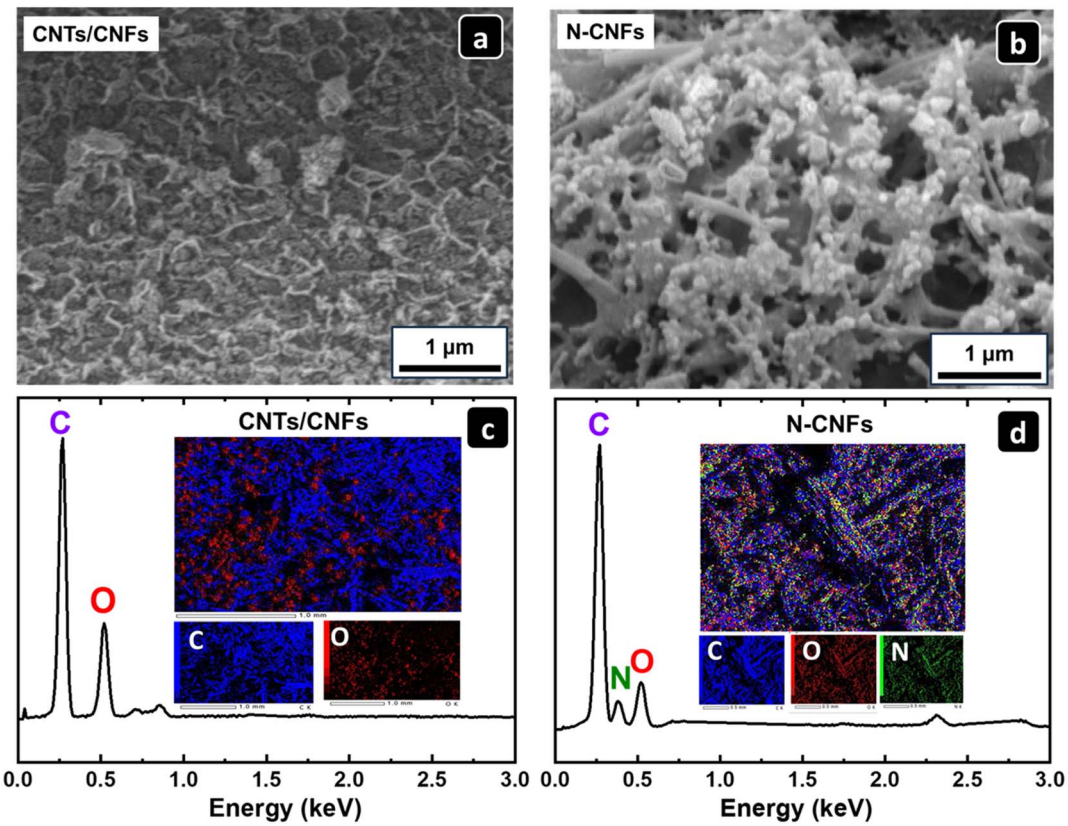

Fig. 1 SEM images and EDS for (a and c) CNTs/CNFs and (b and d) N-CNFs, with the inset showing the EDS elemental mapping, respectively.

N-CNFs in Fig. 1b demonstrate a three-dimensional, interconnected network of tubular fibers, along with small, globular particles resembling cauliflower that are uniformly distributed on the N-CNFs and are formed by damaged CNFs during the conversion process. Both CNTs/CNFs exhibit a 3D interconnected structure, which is expected to exhibit good electronic conductivity and to form a porous network, thereby improving ion diffusion.

The EDS spectrum, shown in Fig. 1c and d, confirms the presence of C and O in the CNTs/CNFs sample, and the existence of C, O, and N in the N-CNFs, with a significant decrease in oxygen content after nitrogen doping. Moreover, the EDS mapping reveals the homogenous distribution of the detected elements in the prepared materials.

The HRTEM image of the CNTs/CNFs in Fig. 2a shows them as randomly oriented, elongated, thin, cylindrical tubes with diameters of 7–13 nm. The HRTEM image in Fig. 2b and its inset show that the N-CNFs maintained their cylindrical shape, with small particles formed by damaged CNFs during the conversion process, confirming observations from the SEM images.

Fig. 2c and d show changes in wettability, as measured by a contact angle test. Even though the EDS analysis in Fig. 1c and d shows a decrease in total oxygen content after nitrogen doping, this reduction in oxygen content is acompined with the introduction of polar nitrogen functionalities, which explains the observed substantial increase in hydrophilicity, with the contact angle decreasing from 19.6° for CNTs/CNFs to nearly zero for N-CNFs.[28]

The XRD patterns shown in Fig. 3a verify the graphitic character of both CNTs/CNFs and N-CNFs. The diffraction peak at 24–26° corresponds to the (002) plane of graphitic carbon, indicating the presence of stacked graphene layers, while the peak near 42–44° corresponds to the (100) plane, representing the in-plane order of hexagonal carbon networks.[29,30] For CNTs/CNFs, sharp (002), (100), and higher-order peaks such as (004) and (110) suggest a greater degree of graphitic crystallinity and more structured carbon domains.[30] Some minor peaks were observed due to traces of the catalyst. Conversely, N-CNFs exhibit broader, less intense diffraction features, notably a widened (002) band, indicative of turbostratic, defect-rich carbon structures.[31] This broadening results from nitrogen incorporation, which distorts the graphitic lattice, alters long-range order, and slightly increases the interlayer distance.[31] Furthermore, the appearance of a low-angle superstructural feature in both samples' patterns indicates mesoscale structural organization, a common trait in nanostructured carbon materials.

The primary functional groups of CNTs/CNFs and N-CNFs samples were examined using FT-IR spectroscopy. For CNTs/CNFs, the FT-IR spectrum in Fig. 3b showed characteristic bands (O–H), (C–H), (C═O), (C═C), (C–O–C), and (C–O) at 3438, 2921, 1634, 1217, 1058, and 596 cm^{-1}, respectively.[32,33] Compared with the spectrum of N-CNFs, new absorption bands at around 1385 and 1100 cm^{-1} related to (C–N) and (N–CH_3), proving the presence of intercalated N atoms between the graphite layers at the inner part of the CNFs.[27] The FTIR spectra indicated that most of the oxygen-containing groups on CNTs/

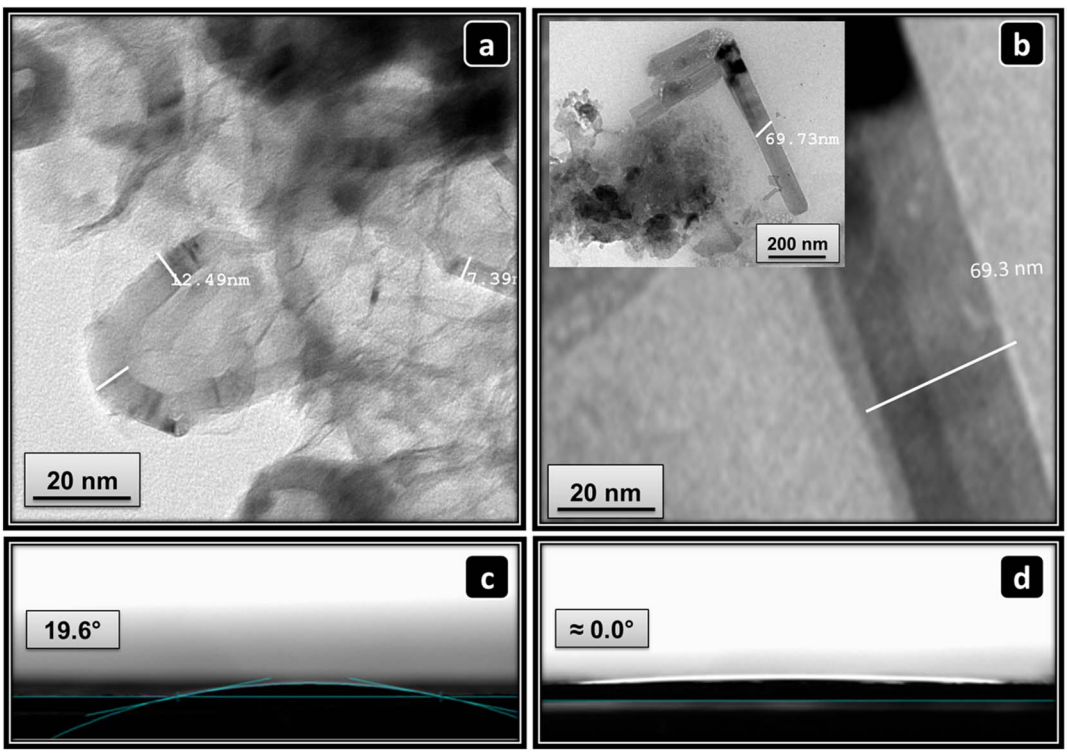

Fig. 2 HRTEM of and contact angle of (a and c) CNTs/CNFs and (b and d) N-CNFs, respectively.

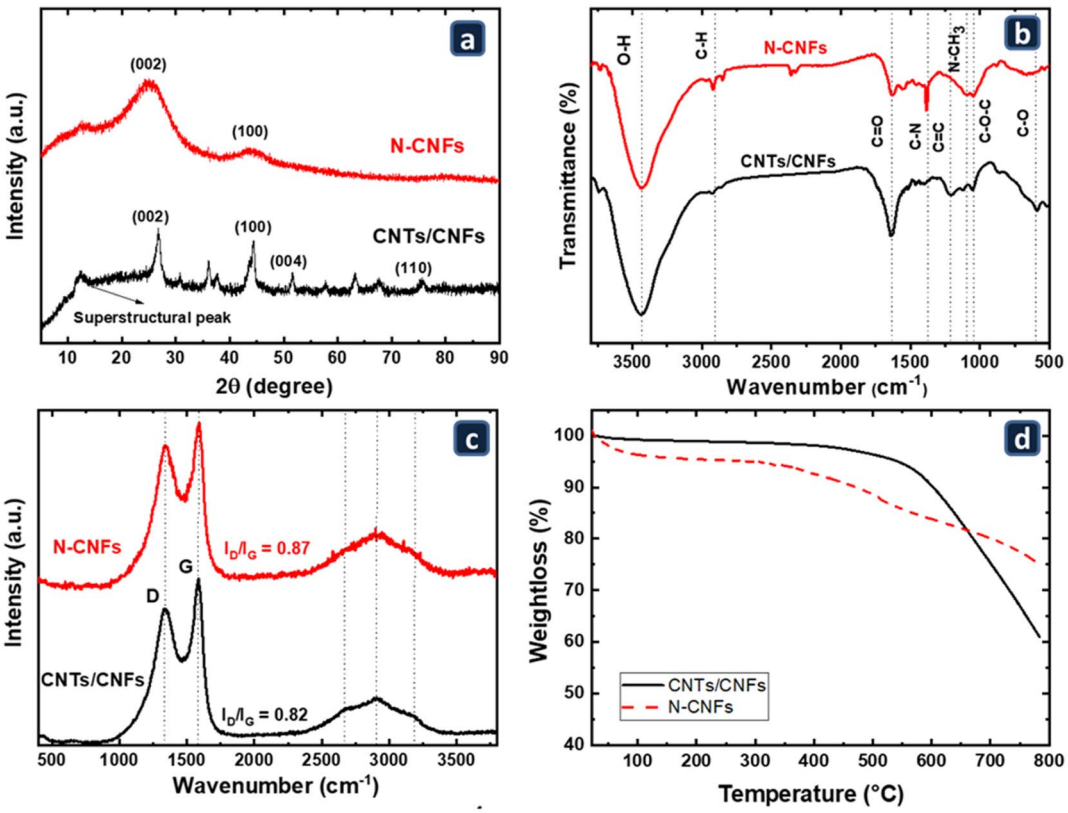

Fig. 3 (a) The XRD patterns, (b) FTIR spectra, (c) Raman spectra, and (d) TGA of the fabricated materials.

CNFs were reduced during the preparation of N-CNFs, as supported by the EDS results (Fig. 1c and d).

The Raman spectra of CNTs/CNFs and N-CNFs samples in Fig. 3c exhibit characteristic D and G bands at ~1339 and 1586 cm^{-1}, respectively, corresponding to the defective (sp^3) and graphitic (sp^2) carbon structures.[34] The intensity ratio (I_D/I_G) is commonly used to evaluate the degree of disorder within carbon materials.[35] CNTs/CNFs show an I_D/I_G ratio of 0.82, indicating a relatively ordered, graphitic structure with limited defects.[34] Upon nitrogen incorporation, N-CNFs display an increased D-band intensity and a higher I_D/I_G ratio of 0.87, reflecting enhanced structural disorder and a reduction in the size of in-plane sp^2 domains due to nitrogen-induced defects.[36] Furthermore, the Raman spectra of CNTs/CNFs and N-CNFs show high-intensity overlapping multi-bands at 2672 (2D), 2904 (D + G combinations), and 3185 cm^{-1} (2G).[37] Broadening of the 2D and 2G bands in the case of the N-CNFs indicates the extra defect-rich nature of the doped nanofibers.[38–40] The presence of various nitrogen species creates a wide distribution of local bond lengths and electronic environments, leading to a range of slightly different vibrational frequencies and, consequently, broader spectral features. Furthermore, the broadened 2D band suggests a loss of long-range graphitic stacking and an increase in layer misalignment (turbostratic arrangement), correlating with the widened (002) peak observed in the XRD patterns.[38] On the other hand, the increased intensity in the D + G region of the N-CNF spectrum indicates the presence of additional defects induced by doping. In disordered or heteroatom-doped carbons, this band becomes intense because defects and dopants enhance double-resonant combination scattering compared with pristine crystalline graphite.[41] Overall, the Raman analysis confirms that CNTs/CNFs possess a more graphitic framework, whereas N-CNFs exhibit a higher defect density due to nitrogen doping.[42]

Fig. 3d displays the TGA curves of CNTs/CNFs and N-CNFs. CNTs/CNFs exhibit a long plateau, followed by a sharp mass loss as the robust sp^2 framework begins to decompose.[43] In contrast, N-CNFs displayed a mass loss below 100 °C due to the water removal, reflecting their higher hydrophilicity in comparison to CNTs/CNFs, as supported by the contact angle measurements (Fig. 2c and d). In the case of N-CNFs, the incorporation of nitrogen into the carbon nanofiber framework significantly enhances surface wettability by introducing polar nitrogen-containing functionalities (such as pyridinic-*N*, pyrrolic-*N*, and graphitic-*N*). These nitrogen species increase the surface energy and improve the affinity of the carbon surface toward aqueous electrolytes through strong dipole–dipole and donor–acceptor interactions, even when the apparent O–H signal is lower in FTIR spectra, which is sample size dependent. Therefore, the improved hydrophilicity of N-CNFs originates mainly from nitrogen-induced surface polarity and electronic modulation rather than from a higher concentration of oxygenated groups.[44] In addition, an earlier onset of mass loss and a more gradual, multi-stage degradation profile was observed, reflecting the destabilizing effect of nitrogen-induced defects in the graphitic lattice and the sequential

decomposition of different nitrogen species, such as pyridinic and pyrrolic nitrogen, with the graphitic nitrogen remaining the most thermally robust.[45–47]

To investigate the elemental composition and chemical states of CNTs/CNFs and N-CNFs samples, XPS analysis was utilized, and the resulting spectra are illustrated in Fig. 4a–c. In Fig. 4a, the C 1s spectra of the CNTs/CNFs sample showed only two peaks at 284.6 eV and 286.0 eV related to C–C and C–O bonding, respectively. In contrast, for the N-CNFs, the C 1s spectra were deconvoluted into five peaks. At 281.7 and 283.0 eV, two peaks correspond to surface and bulk M–C formed during the CNT/CNFs formation. The other three peaks at 284.6, 286.1, and 288 eV are related to C–C, C–O/C–N, and C=O/C=N bonds, respectively. The presence of these peaks and the slight shift in the C–O/C–N peak indicate the incorporation of nitrogen atoms and the introduction of more defects into the carbon structure.[48,49]

Fig. 4b presents the O 1s spectra of the CNTs/CNFs and N-CNFs materials, both of which show three peaks. For CNTs/CNFs, the peaks at 530.2, 531.6, and 532.5 eV are related to carboxyl (C=O), hydroxyl/carboxylate (C–OH/(O–C=O), and ether (C–O–C) oxygen, respectively. These features indicate the presence of oxygenated defects on the surface of the carbon nanostructure. After nitrogen doping, the O 1s spectrum showed three peaks at 529.0, 531.2, and 534.1 eV. The peak at 529.0 eV is attributed to strongly bound oxygen species, such as M–O (due to traces of catalyst) or C=O, stabilized by neighboring nitrogen atoms. The dominant peak at 531.2 eV corresponds to O=C–O, with a reduced binding energy due to the electron-donating effect of nitrogen dopants. The peak at 534.1 eV is assigned to adsorbed water and to highly polar oxygen environments arising from nitrogen doping.[48,50,51] The presence of that peak in the case of N-CNFs and its absence in the case of CNTS/CNFs indicates the high hydrophilicity of the N-CNFs sample.

In Fig. 4c, the N 1s spectra of the N-CNFs material exhibit three peaks at 399.6, 398.3, and 396.2 eV, respectively. The peak at 396.2 eV is assigned to M–N_x bonding, indicating coordination between nitrogen and residual Fe/Ni catalyst particles. The presence of pyridinic and pyrrolic nitrogen peaks at 398.3 and 399.6 eV, respectively, suggests that nitrogen is incorporated into the carbon lattice and at the defect sites.[48,50] The observed broad FWHM of the peaks is likely due to the heterogeneous distribution of nitrogen dopants within the carbon lattice, defects, edges, and vacancies, which inherently broaden the XPS peak.[52]

3.2. Electrochemical characterizations and SC performance

To study the supercapacitive performance of the fabricated samples, cyclic voltammetry (CV) was performed in 0.5 M H_2SO_4 within the potential range of 0.0–1.2 V *vs.* SCE at different scan rates (5–100 mV s^{-1}), and depicted in Fig. 5a and b, with N-CNFs electrodes showing a higher CV area than CNTs/CNFs at all scan rates. Notably, both electrodes exhibited a deviation from the standard rectangular shape due to the presence of EDLC, with extra-broad redox peaks evident at slow scan rates, indicating pseudocapacitive behavior in addition to EDLC. Both CNTs/CNFs and N-CNFs contain oxygen and nitrogen groups, as confirmed by the FT-IR and XPS analysis, which contribute to the observed reversible surface redox reactions and hence to charge storage *via* a pseudocapacitive mechanism. Such behavior is commonly observed in surface functionalized and heteroatom-doped carbon materials and accounts for the enhanced specific capacitance relative to purely electrostatic double-layer systems. For comparison, Fig. 5c shows the CVs of CNTs/CNFs and N-CNFs electrodes at 50 mV s^{-1} in 0.5 M H_2SO_4. The CV area of the N-CNFs electrode is significantly higher than that of the CNTs/CNFs electrode, which can be attributed to the presence of nitrogen atoms that improve both electrical conductivity and hydrophilicity.[53]

Fig. 5d displays the plot of log *I versus* log *v*, and the estimated *b* value, calculated from the power law, was 0.58 for CNTs/CNFs and 0.55 for N-CNFs at 0.6 V *vs.* SCE. The *b* values falling between 0.5 and 1 suggest that the charge storage mechanism is controlled by mixed surface and diffusion processes.[54] The closer the value is to 0.5, the more diffusion-controlled the process, while a value close to 1 indicates a non-diffusion-controlled (capacitive) process. According to the obtained values, the SC behavior of the synthesized materials is diffusion controlled.

To analyze the capacitive and diffusion-controlled contributions in the 3-electrode system, using eqn (3) and (4) (Dunn/Trasatti Method).[55]

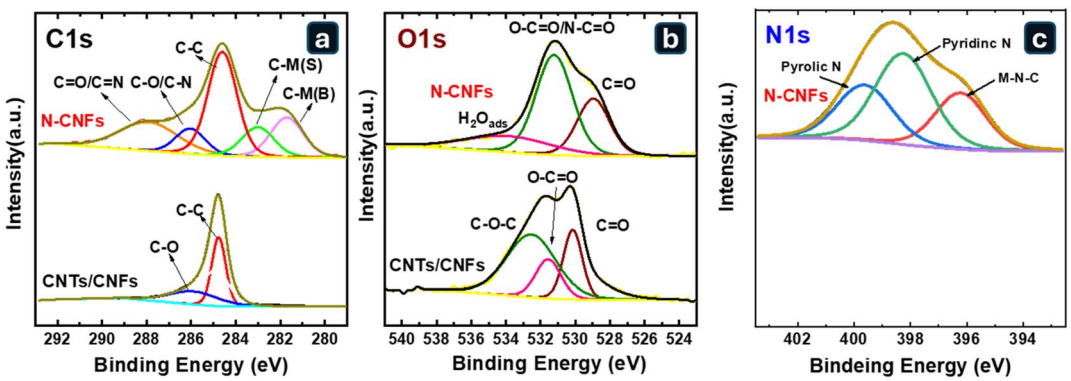

Fig. 4 (a) C 1s, (b) O 1s, and (c) N 1s XPS spectra of the fabricated CNTs/CNFs and (N-CNFs).

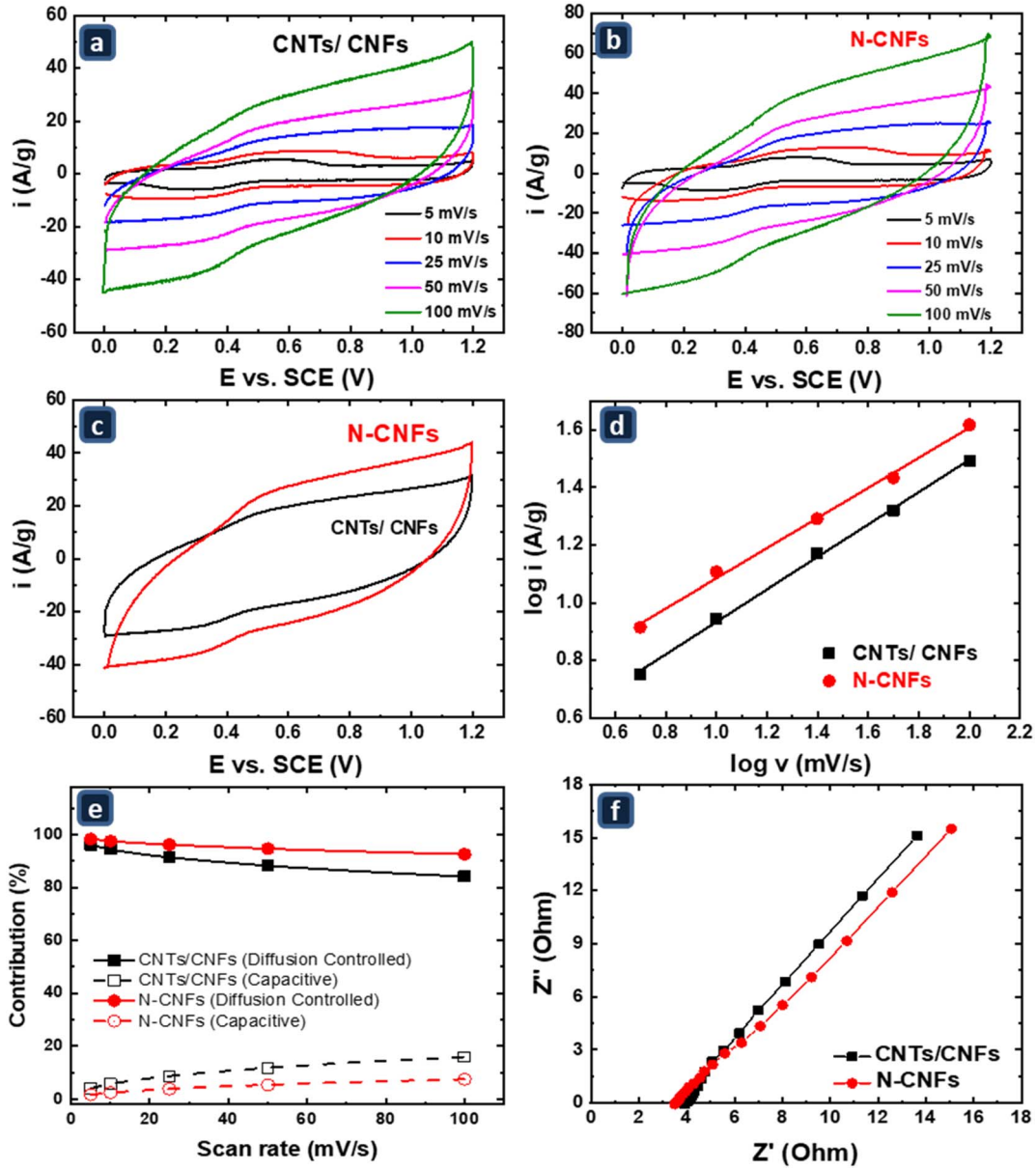

Fig. 5 (a and b) Cyclic voltammetry (CV) measurements of CNTs/CNFs and N-CNFs electrodes at various 5–100 mV scan rates, respectively, and (c) CVs of CNTs/CNFs and N-CNFs electrodes at a scan rate of 50 mV s^{-1}, all in 0.5 M H_2SO_4 at RT. (d) The power-law relationship between the log I and the log ν was investigated at 0.6 V. (e) The contributions of capacitive and diffusion-controlled charge storage were determined for CNTs/CNF and N-CNF electrodes. (f) Nyquist plot of the EIS measurements at open circuit potential.

$$I(\mathrm{v}) = K_1\,\nu + K_2\,\nu^{0.5} \quad (3)$$

$$I(\mathrm{v})/\nu^{0.5} = K_1\,\nu^{0.5} + K_2 \quad (4)$$

where $(K_1\,\nu)$ and $(K_2\,\nu^{0.5})$ represent the non-diffusion-controlled (surface or capacitive) current contribution and diffusion-controlled current contribution, respectively. The values of K_1 and K_2 are intended by profiling the $I(\mathrm{v})/\nu^{0.5}$ *vs.* $\nu^{0.5}$ curves. The contributions of capacitive and diffusion-controlled charge storage for the CNTs/CNFs and N-CNFs electrodes are depicted in Fig. 5e. It is clear that most of the charge storage is ascribed to the diffusion-controlled process.[56] At slow scan rates, 95.9% of the current for the CNTs/CNFs electrode was attributed to the diffusion-controlled component, indicating greater access to the bulk of the material. As the scan rate increases, this contribution drops to 83.7%, indicating less bulk accessibility. In the case of N-CNFs, it drops from 98.9% to only 92.4%, indicating greater bulk accessibility during charging, due to its higher wettability.[57] To further investigate the diffusion-controlled characteristics of the CNTs/CNFs and N-CNFs, EIS was employed, and the Nyquist plot is illustrated in Fig. 5f. The two samples exhibited minimal ohmic resistance (R_s) values of 3.96 and 3.52 ohms, respectively, indicating their excellent conductivity. A distinct linear region with a slope of $\approx$1.5 is observed at both high and low frequencies in both samples, reflecting a dominant diffusion-limited capacitance behavior.

To comprehensively investigate the SC behavior of CNTs/CNFs and N-CNFs, galvanostatic charge–discharge (GCD) measurements are crucial. The C_s at different current densities were calculated from the GCD graphs using eqn (5), where m represents the mass of the active materials in g, I is the current density in A g^{-1}, ΔV is the potential scale in V, and Δt is the discharging time in seconds.

$$C_s = (I\Delta t)/(m\Delta V) \quad (5)$$

Fig. 6a shows the GCD measurements of N-CNFs electrodes at charging/discharging rates of 1–10 A g^{-1} in the potential range of 0.0–1.2 V *vs.* SCE, as an example, while Fig. 6b compares the GCD of CNTs/CNFs and N-CNFs electrodes at a current density of 2 A g^{-1}.

The GCD curves in Fig. 6a exhibit a quasi-triangular shape, indicating high electrical conductivity and facilitating rapid charge transfer.[58,59] In Fig. 6b, the N-CNFs electrode demonstrates a superior specific capacitance of 1093 F g^{-1}, ≈1.6 times that of CNTs (670 F g^{-1}) at 2 A g^{-1}. This significant performance improvement is primarily attributed to nitrogen functionalization, such as pyridinic-*N*, pyrrolic-*N*, and M–N_x that increase surface polarity, facilitate electron transfer, and promote ion adsorption. This is further evidenced by the dramatic decrease in contact angle from 19.6° for CNTs/CNFs to nearly zero for N-CNFs, confirming improved hydrophilicity,[48,57,60] leading to superior performance in supercapacitors that is much higher than previously reported for carbon-based materials (Table 1).

Fig. 6c shows that as the GCD current density increases, the C_s value decreases in both samples, but to different extents. For CNTs/CNFs, the C_s decreased from 800 to 507 F g^{-1} with an increase in current density from 1 to 10 A g^{-1}, maintaining 63% of its highest capacitance. For N-CNTs, the C_s decreased from 1283 to 780 F g^{-1}, maintaining 61% of its maximum capacitance. However, in general, the C_s values for the N-CNFs are significantly higher than those for CNTs/CNFs at all current densities.

Fig. 6d displays the number of electrochemically active sites, calculated at 1 A g^{-1}, using eqn (6), where Q_s is the total charge density (C g^{-1}), e is the elementary charge of an electron (1.602×10^{-19} C), and N is Avogadro's number (6.022×10^{23} mol^{-1}).[4] The number of active sites is 10 mmol g^{-1} and 16 mmol g^{-1} for CNTs/CNFs and N-CNFs, respectively, confirming the superior performance of the N-CNF electrode.

$$\text{Molar of active sites per gram} = Q_s\ (\text{C g}^{-1})/eN \quad (6)$$

As the N-CNFs electrode showed the best performance in the three-electrode measurements, its performance in a two-electrode system was further explored using a symmetrical two-electrode device with 0.5 M H_2SO_4 electrolyte. Fig. 7a shows the CVs of the N-CNF device at different scan rates, indicating a 1.5 V potential window with no faradaic currents. In addition,

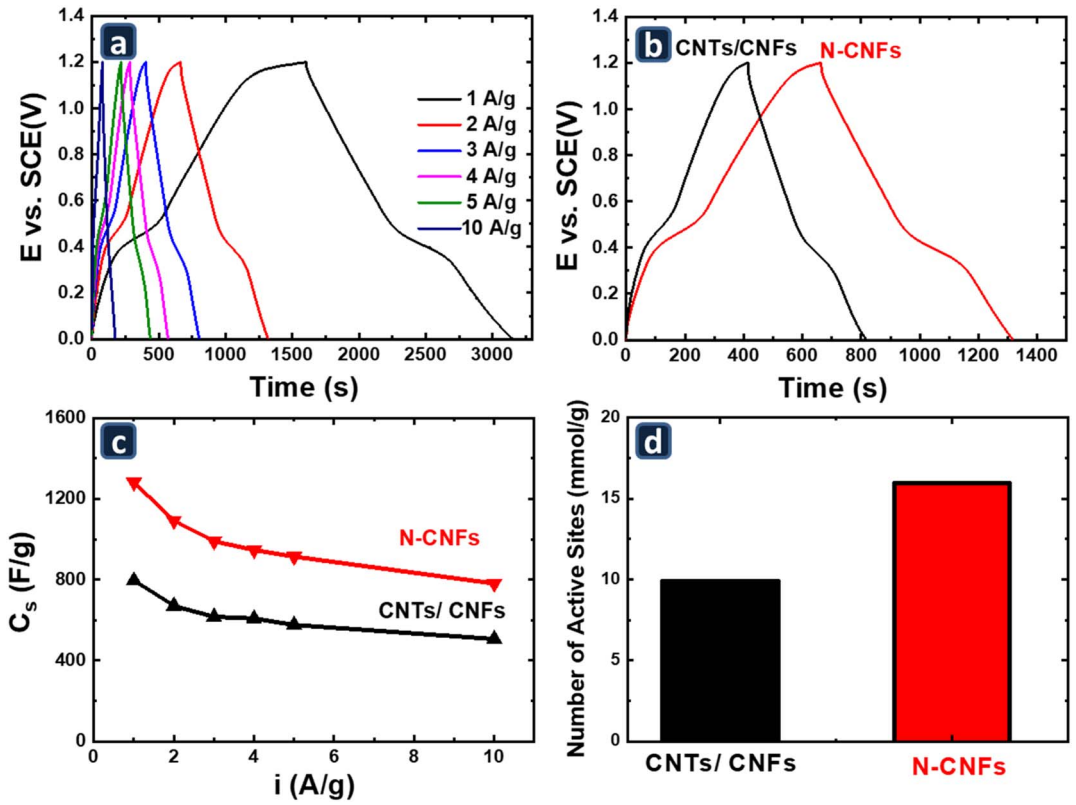

Fig. 6 (a) GCD measurements of N-CNFs electrodes at different current densities of 1–10 A g^{-1}, and (b) GCD of CNTs/CNFs and N-CNFs electrodes at charge/discharge current density of 2 A g^{-1}, all in 0.5 M H_2SO_4 at RT. (c) average C_s of CNTs and N-CNFs electrodes at various current densities. (d) The number of electrochemically active sites in CNTs and N-CNFs electrodes at 5 mV s^{-1}.

Table 1 Comparison of the obtained specific capacitance of CNTs/CNFs and N-CNFs in this study with those reported in the literature for similar carbon-based electrodes

Material	Electrolyte	Specific capacitance (F g^{-1})	Ref.
Dense-packed CNT spherical	1.0 M H_2SO_4	215 (0.2 A g^{-1})	14
A carbon-coated g-C_3N_4 nanotubes (C-TCN)	1 M KOH	242 (1 A g^{-1})	48
CNTs/GNF_s	6 M KOH	270 (1 A g^{-1})	59
N-doped porous RGO	1 M H_2SO_4	103.2 (100 mv s^{-1})	60
One-dimensional hierarchically porous carbon	6 M KOH	256 (5 mV s^{-1})	61
N-CNTs	1.0 M H_2SO_4	263 (1 A g^{-1})	62
N-doped porous carbon nanotubes derived from polypyrene (NCNs-A)	6 M KOH	285 (0.5 A g^{-1})	63
N, P/CNT	1.0 M H_2SO_4	358 (0.5 A g^{-1})	64
N-doped crumpled carbon nanotubes	6 M KOH	336 (0.5 A g^{-1})	65
CNT@m-C	6 M KOH	178 (2 A g^{-1})	66
Human hair-derived carbon (HMCs)	6 M KOH	340 (1 A g^{-1})	67
CNTs/CNFs	0.5 M H_2SO_4	800 F g^{-1} (1 A g^{-1})	This work
N-CNFs)	0.5 M H_2SO_4	1283 (1 A g^{-1})	This work

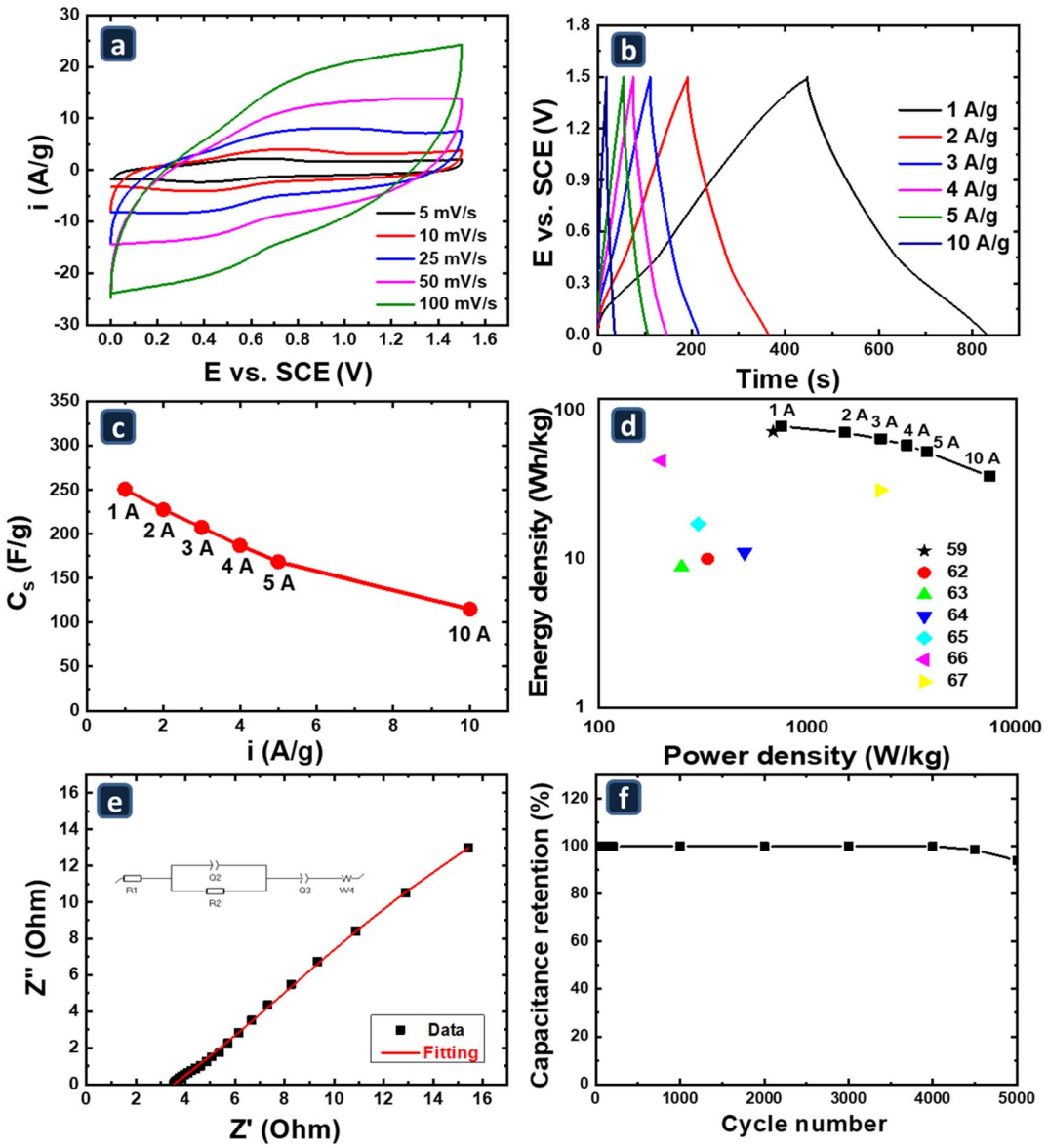

Fig. 7 Electrochemical properties of the N-CNFs symmetric two-electrode device, all in 0.5 M H_2SO_4. (a) CVs at scan rates of 5–100 mV s^{-1} and (b) GCD responses at various current densities of 1–10 A g^{-1}. (c) The average specific capacitance (C_s) and (d) the Ragone plot at various current densities in comparison to values from the literature (ref. 59 and 62–67). (e) The Nyquist plot of the EIS results at OCP (inset: an equivalent circuit was used to fit the experimental results). (f) Capacitance retention for 5000 GCD cycles at 10 A g^{-1}.

distinct pseudocapacitive behavior is observed at low potentials, especially at slow scan rates. The GCD results at different current densities are shown in Fig. 7b and exhibit a quasi-triangular shape, with no sign of IR drop or plateaus, which are indicative of resistance or faradaic reactions, respectively. Indicating high electrical conductivity and facilitating rapid charge transfer. In addition, a change in the slope is observed at low potentials, indicating the pseudocapacitive behavior, which matches the CV results. Doping carbon nanofibers with nitrogen, along with the presence of oxygen- and nitrogen-based surface functional groups and defects, enhanced redox reactions and boosted charge density through a pseudocapacitive contribution.[68,69]

Fig. 7c shows the calculated C_s values at each current density. Increasing the current density decreased the C_s value from 251 to 115 F g^{-1}, maintaining only 46% of the maximum capacitance, a significant drop compared to the three-electrode measurements (61%). This behavior is expected as the two-electrode system is known to suffer from further ion-diffusion limitations.

The energy (E in Wh kg^{-1}) and power (P in W kg^{-1}) densities are calculated from the GCD plots using eqn (7) and (8), where, C_s is the specific capacitance calculated from the charge/discharge curves, I is the discharge current (A), t is the discharge time (h), ΔV is the potential window (V), and m is the mass of the (N-CNFs) electrode (kg).

$$E = \frac{1}{2}C_s(\Delta V)^2 = \frac{I\Delta V t}{2m} \quad (7)$$

$$P = \frac{E}{t} = \frac{I\Delta V}{m} \quad (8)$$

The calculated E and P were presented in Ragone's plot in Fig. 7d. The assembled symmetric N-CNF supercapacitor delivers an energy density of 78.3 Wh kg^{-1} and a power density of 750 W kg^{-1} at a current density of 1 A g^{-1}, while at 10 A g^{-1}, E of 36 Wh kg^{-1} and P of 7500 W kg^{-1} are reported, implying rapid ion and electron propagation. The energy density of the N-CNFs supercapacitor is higher than that reported for carbon-based electrodes examined under similar conditions.[59,62–67]

Fig. 7e displays the Nyquist plots of the N-CNFs two-electrode device at OCP. An R_s value of approximately 3.4 ohms is obtained, representing the series resistance, including electrolyte and active material/current collector contact resistances.[70] An R_{ct} value of 0.21 ohm, as indicated by the small semicircle, indicates that the electrode materials exhibit fast redox reaction kinetics. This performance is attributed to the presence of nitrogen, which enhances electrical conductivity and wettability and provides further functional groups to the surface. Additionally, at low frequencies, the Warburg behavior, with a slope of 1.07, dominates the EIS response and indicates a major contribution from diffusion, as confirmed by three- and two-electrode measurements.[71]

The cycle-life test of the N-CNFs electrode involved GCD measurements at 10 A g^{-1} for 5000 cycles, as depicted in Fig. 7f. 100% capacitance retention with a coulombic efficiency of 95% is achieved up to 4000 cycles, underscoring the excellent cycling stability of the N-CNFs electrodes. The slight drop to 95% after 5000 cycles is most likely due to the membrane drying rather than any degradation of the electrode materials, as carbon materials are known to have capacity retention up to 20 000 cycles.[72]

4. Conclusion

The CNTs/CNFs were prepared using an eco-friendly method from recycling pinewood sawdust (PWSD). The prepared CNTs/CNFs were treated with urea to produce nitrogen-doped carbon nanofibers (N-CNFs). The incorporation of nitrogen into the carbon frame and the conversion of CNTs/CNFs to more amorphous N-CNFs with nitrogen groups are confirmed by FTIR, XRD, TGA, and XPS analysis. High-resolution transmission electron microscopy (HRTEM) revealed the formation of N-CNFs with a fiber-like structure and the presence of some ultrasonication-induced flakes. The contact angle was reduced significantly from 19.6 for the CNTs/CNFs to zero for (N-CNFs), indicating a substantial increase in hydrophilicity after N-doping and the formation of N-CNFs. The N-CNFs electrode demonstrated a maximum specific capacitance of 1283 F g^{-1} at a current density of 1 A g^{-1} in the three-electrode setup. A symmetric device of N-CNFs exhibited a maximum specific capacitance of 251 F g^{-1}, an energy density of 78.325 Wh kg^{-1}, and a power density of 750 W kg^{-1} at 1 A g^{-1}. Furthermore, excellent cycling retention of 99.9% up to 4500 at 10 A g^{-1}. The observed high performance of this nanocomposite, compared to bare CNTs/CNFs, can be attributed to the advantages of nitrogen doping, which provides more active sites, increased hydrophilicity, and excellent chemical stability.

Conflicts of interest

There are no conflicts to declare.

Data availability

All data supporting this article are included in the article.

Acknowledgements

We highly appreciate the financial support for our existing work from the American University in Cairo and the National Research Centre.

References

1 D. M. El-Gendy, R. M. A. E. Wahab, M. M. Selim and N. K. Allam, A facile synthesis of zeolitic analcime/spongy graphene nanocomposites as novel hybrid electrodes for symmetric supercapacitors, *J. Energy Storage*, 2020, **32**, 101953, DOI: 10.1016/j.est.2020.101953.
2 D. M. El-Gendy, N. A. Abdel Ghany and N. K. Allam, Black titania nanotubes/spongy graphene nanocomposites for

high-performance supercapacitors, *RSC Adv.*, 2019, **9**, 12555–12566, DOI: 10.1039/C9RA01539F.

3 D. M. El-Gendy, N. A. Abdel Ghany and N. K. Allam, Synergistic effect of silver and adenine on boosting the supercapacitance performance of spongy graphene, *J. Energy Storage*, 2019, **24**, 100776, DOI: 10.1016/j.est.2019.100776.

4 D. M. El-Gendy, N. K. Allam and E. N. El Sawy, Novel high energy density electrodes based on functionalized/exfoliated molybdenum oxide nanoflakes for high-performance supercapacitors, *Mater. Today Chem.*, 2023, **29**, 101414.

5 D. Shan, J. Yang, W. Liu, J. Yan and Z. Fan, Biomass-derived three-dimensional honeycomb-like hierarchical structured carbon for ultrahigh energy density asymmetric supercapacitors, *J. Mater. Chem. A*, 2016, **4**, 13589–13602.

6 R. A. M. Adam, D. J. Tarimo, V. M. Maphiri, A. A. Mirghni, O. Fasakin and N. Manyala, Effects of the physisorption properties of human hair-derived activated carbon as a potential electrode for symmetric supercapacitor, *Mater. Renew. Sustain. Energy*, 2025, **14**, 22, DOI: 10.1007/s40243-024-00294-3.

7 Y. Yuan, J. Zhou, M. I. Rafiq, S. Dai, J. Tang and W. Tang, Growth of NiMn layered double hydroxide and polypyrrole on bacterial cellulose nanofibers for efficient supercapacitors, *Electrochim. Acta*, 2019, **295**, 82–91, DOI: 10.1016/j.electacta.2018.10.090.

8 A. A. Mirghni, K. O. Oyedotun, B. A. Mahmoud, O. Fasakin, D. J. Tarimo and N. Manyala, A study of Co-Mn phosphate supported with graphene foam as promising electrode materials for future electrochemical capacitors, *Int. J. Energy Res.*, 2022, **46**, 3080–3094, DOI: 10.1002/er.7365.

9 A. Heiba, R. Abou Shahba, A. Dhmees, F. Taher and E. N. El Sawy, Graphene Oxide Nanoribbons (GONRs) As pH-tolerant Electrodes for Supercapacitors: Effect of Charge Carriers and Loading, *J. Energy Storage*, 2024, **83**, 110762–110775, DOI: 10.1016/j.est.2024.110762.

10 Y. Zhou, Q. Li, T. Lu, Y. Zhang, W. He, E. Zhang, C. Liu, X. Wang, Z. Li, Y. Zhu and B. Xu, Rational Design of Three-Dimensional Architectures of Carbon Nanorods/Carbon Nanofibers Composite for High-Performance Supercapacitors, *ACS Appl. Energy Mater.*, 2025, **8**, 1414–1419, DOI: 10.1021/acsaem.4c03006.

11 D. M. El-Gendy, N. A. A. Ghany, E. E. F. El Sherbini and N. K. Allam, Adenine-functionalized Spongy Graphene for Green and High-Performance Supercapacitors, *Sci. Rep.*, 2017, **7**, 43104, DOI: 10.1038/srep43104.

12 R. Isci, K. B. Donmez, N. Karatepe and T. Ozturk, High-Performance Thienothiophene and Single Wall Carbon Nanotube-Based Supercapacitor as a Free-Standing and Flexible Hybrid Energy Storage Material, *ACS Appl. Energy Mater.*, 2024, **7**, 1488–1494, DOI: 10.1021/acsaem.3c02737.

13 T. Lim, B. H. Seo, S. J. Kim, S. Han, W. Lee and J. W. Suk, Nitrogen-Doped Activated Hollow Carbon Nanofibers with Controlled Hierarchical Pore Structures for High-Performance, Binder-Free, Flexible Supercapacitor Electrodes, *ACS Omega*, 2024, **9**, 8247–8254, DOI: 10.1021/acsomega.3c08952.

14 D. Gueon and J. H. Moon, Nitrogen-Doped Carbon Nanotube Spherical Particles for Supercapacitor Applications: Emulsion-Assisted Compact Packing and Capacitance Enhancement, *ACS Appl. Mater. Interfaces*, 2015, **7**, 20083–20089, DOI: 10.1021/acsami.5b05231.

15 J.-R. Zhao, J. Hu, J.-F. Li and P. Chen, N-doped carbon nanotubes derived from waste biomass and its electrochemical performance, *Mater. Lett.*, 2020, **261**, 127146, DOI: 10.1016/j.matlet.2019.127146.

16 W. Qian, F. Sun, Y. Xu, L. Qiu, C. Liu, S. Wang and F. Yan, Human hair-derived carbon flakes for electrochemical supercapacitors, *Energy Environ. Sci.*, 2014, **7**, 379–386, DOI: 10.1039/C3EE43111H.

17 K. A. Adegoke, O. O. Adesina, O. A. Okon-Akan, O. R. Adegoke, A. B. Olabintan, O. A. Ajala, H. Olagoke, N. W. Maxakato and O. S. Bello, Sawdust-biomass based materials for sequestration of organic and inorganic pollutants and potential for engineering applications, *Curr. Res. Green Sustain. Chem.*, 2022, **5**, 100274, DOI: 10.1016/j.crgsc.2022.100274.

18 S. Lei, P. Hu, W. Ruan, Y. Ye, Z. Zheng, S. Li, D. Wang and D. Wang, Influence of one-pot and two-step preparation on the quality of carbon nanotubes using pine sawdust as the catalyst support, *Diam. Relat. Mater.*, 2023, **138**, 110250, DOI: 10.1016/j.diamond.2023.110250.

19 C. Quan, R. Su and N. Gao, Preparation of activated biomass carbon from pine sawdust for supercapacitor and CO2 capture, *Int. J. Energy Res.*, 2020, **44**, 4335–4351, DOI: 10.1002/er.5206.

20 J. Wang, Y. Shang, Y. Xiong and S. Zhang, An insight into biomass-derived low-cost biochar supported FeNi3/NiFe2O4 catalyst: Effect of hydrothermal treatment and carbothermal reduction temperature, *Renewable Energy*, 2025, **246**, 122920, DOI: 10.1016/j.renene.2025.122920.

21 W.-J. Liu, K. Tian, Y.-R. He, H. Jiang and H.-Q. Yu, High-Yield Harvest of Nanofibers/Mesoporous Carbon Composite by Pyrolysis of Waste Biomass and Its Application for High Durability Electrochemical Energy Storage, *Environ. Sci. Technol.*, 2014, **48**, 13951–13959, DOI: 10.1021/es504184c.

22 C. N. R. Rao, A. Govindaraj and L. S. Panchakarla, *Nanotubes and Nanowires*, 2021. doi: DOI: 10.1039/9781788019637-00001.

23 H.-A. S. Tohamy, M. El-Sakhawy and M. M. M. Elnasharty, Carboxymethyl cellulose membranes blended with carbon nanotubes/Ag nanoparticles for eco-friendly safer lithium-ion batteries, *Diam. Relat. Mater.*, 2023, **138**, 110205, DOI: 10.1016/j.diamond.2023.110205.

24 D. Li, X. Duan, H. Sun, J. Kang, H. Zhang, M. O. Tade and S. Wang, Facile synthesis of nitrogen-doped graphene via low-temperature pyrolysis: The effects of precursors and annealing ambience on metal-free catalytic oxidation, *Carbon*, 2017, **115**, 649–658, DOI: 10.1016/j.carbon.2017.01.058.

25 A. Misra, P. K. Tyagi, M. K. Singh and D. S. Misra, FTIR studies of nitrogen doped carbon nanotubes, *Diam. Relat.*

Mater., 2006, **15**, 385–388, DOI: 10.1016/j.diamond.2005.08.013.

26 H.-A. S. Tohamy and H. S. Magar, A Flexible, Low-Cost, Disposable Non-Enzymatic Electrochemical Sensor Based on MnO2/Cellulose Nanostructure, *ECS J. Solid State Sci. Technol.*, 2022, **11**, 127003, DOI: 10.1149/2162-8777/acad27.

27 H.-A. S. Tohamy, Cellulosic nitrogen doped carbon quantum dots hydrogels with fluorescence/visco-elastic properties for pH- and temperature-sensitivity, *Diam. Relat. Mater.*, 2023, **136**, 110027, DOI: 10.1016/j.diamond.2023.110027.

28 D. Janas and G. Stando, Unexpectedly strong hydrophilic character of free-standing thin films from carbon nanotubes, *Sci. Rep.*, 2017, **7**, 12274, DOI: 10.1038/s41598-017-12443-y.

29 M. Pietrowski, E. Alwin, M. Zieliński, S. Szunerits, A. Suchora and R. Wojcieszak, In situ growth of N-doped carbon nanotubes from the products of graphitic carbon nitride etching by nickel nanoparticles, *Nanoscale Adv.*, 2024, **6**, 1720–1726, DOI: 10.1039/D3NA00983A.

30 I. Aziz, X. Chen, X. Hu, W. Angela) Zhang, R. J. Awan, A. Rauf and S. N. Arshad, Growth of carbon nanotubes over carbon nanofibers catalyzed by bimetallic alloy nanoparticles as a bifunctional electrode for Zn–air batteries, *RSC Adv.*, 2023, **13**, 11591–11599, DOI: 10.1039/D3RA00352C.

31 Y. Ren, J. Tian, S. Li, X. Li, X. Zhao, X. Wang, P. Yang, J. Ni, X. Ji and P. Liu, Phosphorus and boron enhanced N-doped carbon nanofibers for enhanced lithium ion storage, *RSC Adv.*, 2025, **15**, 19522–19529, DOI: 10.1039/D5RA00982K.

32 H.-A. S. Tohamy, M. El-Sakhawy and S. Kamel, Carbon nanotubes from agricultural wastes: Effective environmental adsorbent, *Egypt. J. Chem.*, 2022, **65**, 437–446, DOI: 10.21608/ejchem.2022.123337.5511.

33 H.-A. S. Tohamy, M. El-Sakhawy and M. M. M. Elnasharty, Carboxymethyl cellulose membranes blended with carbon nanotubes/Ag nanoparticles for eco-friendly safer lithium-ion batteries, *Diam. Relat. Mater.*, 2023, **138**, 110205, DOI: 10.1016/j.diamond.2023.110205.

34 X. Liu, J. Choi, Z. Xu, C. P. Grey, S. Fleischmann and A. C. Forse, Raman Spectroscopy Measurements Support Disorder-Driven Capacitance in Nanoporous Carbons, *J. Am. Chem. Soc.*, 2024, **146**, 30748–30752, DOI: 10.1021/jacs.4c10214.

35 S. Ait Abdelkader, M. Boutahir, A. H. Rahmani, B. Fakrach, M. Bentaleb, H. Chadli and A. Rahmani, Raman spectroscopy analysis of single wall carbon nanotubes with penta- and hexa-vacancies defects, *IOP Conf. Ser. Mater. Sci. Eng.*, 2020, **783**, 012014, DOI: 10.1088/1757-899X/783/1/012014.

36 L. G. Bulusheva, A. V. Okotrub, I. A. Kinloch, I. P. Asanov, A. G. Kurenya, A. G. Kudashov, X. Chen and H. Song, Effect of nitrogen doping on Raman spectra of multi-walled carbon nanotubes, *Phys. Status Solidi B*, 2008, **245**, 1971–1974, DOI: 10.1002/pssb.200879592.

37 N. Solati, S. Mobassem, A. Kahraman, H. Ogasawara and S. Kaya, A comprehensive study on the characteristic spectroscopic features of nitrogen doped graphene, *Appl. Surf. Sci.*, 2019, **495**, 143518, DOI: 10.1016/j.apsusc.2019.07.260.

38 J. Briceño, D. Rosas-Medellín, I. L. Alonso-Lemus and B. Escobar, Nitrogen-doped carbon nanotubes with high-surface-area as electrocatalysts in alkaline media: Enhanced performance and life cycle assessment, *Int. J. Hydrogen Energy*, 2025, **141**, 1153–1164, DOI: 10.1016/j.ijhydene.2025.02.048.

39 L. G. Bulusheva, A. V. Okotrub, I. A. Kinloch, I. P. Asanov, A. G. Kurenya, A. G. Kudashov, X. Chen and H. Song, Effect of nitrogen doping on Raman spectra of multi-walled carbon nanotubes, *Phys. Status Solidi B*, 2008, **245**, 1971–1974, DOI: 10.1002/pssb.200879592.

40 Z. Zafar, Z. H. Ni, X. Wu, Z. X. Shi, H. Y. Nan, J. Bai and L. T. Sun, Evolution of Raman spectra in nitrogen doped graphene, *Carbon*, 2013, **61**, 57–62, DOI: 10.1016/j.carbon.2013.04.065.

41 A. Jorio and R. Saito, Raman spectroscopy for carbon nanotube applications, *J. Appl. Phys.*, 2021, **129**, 021102, DOI: 10.1063/5.0030809.

42 S. Zeng, H. Chen, F. Cai, Y. Kang, M. Chen and Q. Li, Electrochemical fabrication of carbon nanotube/polyaniline hydrogel film for all-solid-state flexible supercapacitor with high areal capacitance, *J. Mater. Chem. A*, 2015, **3**, 23864–23870, DOI: 10.1039/C5TA05937B.

43 E. N. Nxumalo, V. O. Nyamori and N. J. Coville, CVD synthesis of nitrogen doped carbon nanotubes using ferrocene/aniline mixtures, *J. Organomet. Chem.*, 2008, **693**, 2942–2948, DOI: 10.1016/j.jorganchem.2008.06.015.

44 J. Hou, C. Cao, F. Idrees and X. Ma, Hierarchical Porous Nitrogen-Doped Carbon Nanosheets Derived from Silk for Ultrahigh-Capacity Battery Anodes and Supercapacitors, *ACS Nano*, 2015, **9**, 2556–2564, DOI: 10.1021/nn506394r.

45 H. Liu, Y. Zhang, R. Li, X. Sun and H. Abou-Rachid, Thermal and chemical durability of nitrogen-doped carbon nanotubes, *J. Nanoparticle Res.*, 2012, **14**, 1016, DOI: 10.1007/s11051-012-1016-0.

46 E. N. Nxumalo and N. J. Coville, Nitrogen Doped Carbon Nanotubes from Organometallic Compounds: A Review, *Materials*, 2010, **3**, 2141–2171, DOI: 10.3390/ma3032141.

47 C. Shang, M. Li, Z. Wang, S. Wu and Z. Lu, Electrospun Nitrogen-Doped Carbon Nanofibers Encapsulating Cobalt Nanoparticles as Efficient Oxygen Reduction Reaction Catalysts, *ChemElectroChem*, 2016, **3**, 1437–1445, DOI: 10.1002/celc.201600275.

48 Z. Lin, K. Wang, X. Wang, S. Wang, H. Pan, Y. Liu, S. Xu and S. Cao, Carbon-Coated Graphitic Carbon Nitride Nanotubes for Supercapacitor Applications, *ACS Appl. Nano Mater.*, 2020, **3**, 7016–7028, DOI: 10.1021/acsanm.0c01340.

49 D. M. El-Gendy, N. A. Abdel Ghany and N. K. Allam, Green, single-pot synthesis of functionalized Na/N/P co-doped graphene nanosheets for high-performance supercapacitors, *J. Electroanal. Chem.*, 2019, **837**, 30–38, DOI: 10.1016/j.jelechem.2019.02.009.

50 O. López-Rojas, Ma. del Socorro Aguilar, J. de Jesús Ku-Herrera, R. M. Jiménez-Barrera, V. H. López, J. García, E. Reyes-Francis, I. Zarazúa and T. López-Luke,

Photoelectrochemical Study of the Performance Enhancement of CNT-Based Counter Electrodes by Adding N-S Doped rGO in QD Solar Cells, *J. Electron. Mater.*, 2025, **54**, 1141–1156, DOI: 10.1007/s11664-024-11606-8.

51 D. Rosenthal, M. Ruta, R. Schlögl and L. Kiwi-Minsker, Combined XPS and TPD study of oxygen-functionalized carbon nanofibers grown on sintered metal fibers, *Carbon*, 2010, **48**, 1835–1843, DOI: 10.1016/j.carbon.2010.01.029.

52 R. Du, N. Zhang, J. Zhu, Y. Wang, C. Xu, Y. Hu, N. Mao, H. Xu, W. Duan, L. Zhuang, L. Qu, Y. Hou and J. Zhang, Nitrogen-Doped Carbon Nanotube Aerogels for High-Performance ORR Catalysts, *Small*, 2015, **11**, 3903–3908, DOI: 10.1002/smll.201500587.

53 D. M. El-Gendy, N. A. A. Ghany, E. F. El Sherbini and N. K. Allam, Adenine-functionalized spongy graphene for green and high-performance supercapacitors, *Sci. Rep.*, 2017, **7**, 43104.

54 A. Elgendy, N. M. El Basiony, F. El-Taib Heakal and A. E. Elkholy, Mesoporous Ni-Zn-Fe layered double hydroxide as an efficient binder-free electrode active material for high-performance supercapacitors, *J. Power Sources*, 2020, **466**, 228294, DOI: 10.1016/j.jpowsour.2020.228294.

55 S. Harish and P. U. Sathyakam, Dunn's Method for Distinguishing Charge Storage Mechanisms in Supercapacitors: A Status Quo Review, *J. Electron. Mater.*, 2025, **54**, 10858–10872, DOI: 10.1007/s11664-025-12481-7.

56 D. M. El-Gendy, N. K. Allam and E. N. El Sawy, Novel high energy density electrodes based on functionalized/exfoliated molybdenum oxide nanoflakes for high-performance supercapacitors, *Mater. Today Chem.*, 2023, **29**, 101414, DOI: 10.1016/j.mtchem.2023.101414.

57 P. Chaluvachar, Y. N. Sudhakar, G. T. Mahesha, V. G. Nair, N. Desai and D. K. Pai, Emerging role of graphitic carbon nitride in advanced supercapacitors: A comprehensive review, *J. Energy Chem.*, 2025, **103**, 498–524, DOI: 10.1016/j.jechem.2024.11.075.

58 H. Ma, Z. Chen, X. Gao, W. Liu and H. Zhu, 3D hierarchically gold-nanoparticle-decorated porous carbon for high-performance supercapacitors, *Sci. Rep.*, 2019, **9**, 17065, DOI: 10.1038/s41598-019-53506-6.

59 Y. Zhou, P. Jin, Y. Zhou and Y. Zhu, High-performance symmetric supercapacitors based on carbon nanotube/graphite nanofiber nanocomposites, *Sci. Rep.*, 2018, **8**, 9005, DOI: 10.1038/s41598-018-27460-8.

60 S. H. Lee, H. W. Kim, J. O. Hwang, W. J. Lee, J. Kwon, C. W. Bielawski, R. S. Ruoff and S. O. Kim, Three-Dimensional Self-Assembly of Graphene Oxide Platelets into Mechanically Flexible Macroporous Carbon Films, *Angew. Chem., Int. Ed.*, 2010, **49**, 10084–10088, DOI: 10.1002/anie.201006240.

61 C. Liang, J. Bao, C. Li, H. Huang, C. Chen, Y. Lou, H. Lu, H. Lin, Z. Shi and S. Feng, One-dimensional hierarchically porous carbon from biomass with high capacitance as supercapacitor materials, *Microporous Mesoporous Mater.*, 2017, **251**, 77–82, DOI: 10.1016/j.micromeso.2017.05.044.

62 R. Rajamanickam, B. Ganesan, I. Kim, I. Hasan, P. Arumugam and S. Paramasivam, Effective synthesis of nitrogen doped carbon nanotubes over transition metal loaded mesoporous catalysts for energy storage of supercapacitor applications, *Z. Phys. Chem.*, 2024, **238**, 1835–1861, DOI: 10.1515/zpch-2023-0458.

63 S. Zong, Y. Zhang, M. S. Xaba, X. Liu and A. Chen, N-doped porous carbon nanotubes derived from polypyrrole for supercapacitors with high performance, *J. Anal. Appl. Pyrolysis*, 2020, **152**, 104925, DOI: 10.1016/j.jaap.2020.104925.

64 J. Devarajan and P. Arumugam, Nitrogen and phosphorous co-doped carbon nanotubes for high-performance supercapacitors, *Carbon Lett.*, 2023, **33**, 1615–1627.

65 S. Zong, J. Du, A. Chen, X. Gao, K. O. Otun, X. Liu and L. L. Jewell, N-doped crumpled carbon nanotubes as advanced electrode material for supercapacitor, *J. Alloys Compd.*, 2022, **928**, 167222, DOI: 10.1016/j.jallcom.2022.167222.

66 Y. Yang, P. Li, S. Wu, X. Li, E. Shi, Q. Shen, D. Wu, W. Xu, A. Cao and Q. Yuan, Hierarchically designed three-dimensional macro/mesoporous carbon frameworks for advanced electrochemical capacitance storage, *Angew. Chem.*, 2015, **21**, 6157–6164, DOI: 10.1002/chem.201406199.

67 W. Qian, F. Sun, Y. Xu, L. Qiu, C. Liu, S. Wang and F. Yan, Human hair-derived carbon flakes for electrochemical supercapacitors, *Energy Environ. Sci.*, 2014, **7**, 379–386, DOI: 10.1039/C3EE43111H.

68 Z. Lin, K. Wang, X. Wang, S. Wang, H. Pan, Y. Liu, S. Xu and S. Cao, Carbon-Coated Graphitic Carbon Nitride Nanotubes for Supercapacitor Applications, *ACS Appl. Nano Mater.*, 2020, **3**, 7016–7028, DOI: 10.1021/acsanm.0c01340.

69 P. Chaluvachar, Y. N. Sudhakar, G. T. Mahesha, V. G. Nair, N. Desai and D. K. Pai, Emerging role of graphitic carbon nitride in advanced supercapacitors: A comprehensive review, *J. Energy Chem.*, 2025, **103**, 498–524, DOI: 10.1016/j.jechem.2024.11.075.

70 D. Momodu, A. Bello, K. Oyedotun, F. Ochai-Ejeh, J. Dangbegnon, M. Madito and N. Manyala, Enhanced electrochemical response of activated carbon nanostructures from tree-bark biomass waste in polymer-gel active electrolytes, *RSC Adv.*, 2017, **7**, 37286–37295, DOI: 10.1039/C7RA05810A.

71 Y. Zhang and E. Xie, Functionalized and tip-open carbon nanotubes for high-performance symmetric supercapacitors, *Dalton Trans.*, 2021, **50**, 12982–12989, DOI: 10.1039/D1DT02055B.

72 M. Jafari and G. G. Botte, Sustainable Green Route for Activated Carbon Synthesis from Biomass Waste for High-Performance Supercapacitors, *ACS Omega*, 2024, **9**, 13134–13147, DOI: 10.1021/acsomega.3c09438.